Investigating the effect of different impurities on plasma detachment in linear plasma machine Magnum-PSI

Physics of Plasmas

Investigating the effect of different impurities on plasma detachment in linear plasma machine Magnum-PSI

Cite as: Phys. Plasmas **26**, 102502 (2019); https://doi.org/10.1063/1.5120180
Submitted: 17 July 2019 . Accepted: 11 September 2019 . Published Online: 01 October 2019

R. Perillo, R. Chandra, G. R. A. Akkermans, I. G. J. Classen, S. Q. Korving, and Magnum-PSI Team

Physics of Plasmas ARTICLE scitation.org/journal/php

Investigating the effect of different impurities on plasma detachment in linear plasma machine Magnum-PSI

Cite as: Phys. Plasmas **26**, 102502 (2019); doi: 10.1063/1.5120180
Submitted: 17 July 2019 · Accepted: 11 September 2019 ·
Published Online: 1 October 2019

R. Perillo, R. Chandra, G. R. A. Akkermans, I. G. J. Classen, S. Q. Korving, and Magnum-PSI Team

AFFILIATIONS

DIFFER—Dutch Institute for Fundamental Energy Research, De Zaale 20, 5612AJ Eindhoven, The Netherlands

ABSTRACT

To achieve a tolerable heat and particle flux to the divertor target of fusion reactors, the so-called plasma detachment is essential to be set up and controlled. Impurity seeding facilitates the achievement of such a regime, mostly due to the enhanced plasma radiation led by the excitation-relaxation cycle of such species. Little is known about the impurity-induced plasma chemical processes occurring in the divertor region during detachment operation. In this work, the influence of three different impurities, i.e., N_2, Ar, and He, on detachment performance is studied. To do so, experimental campaigns on the linear plasma machine Magnum-PSI have been carried out. Results highlight the beneficial role of $N_2 + H_2$ seeding, decreasing the plasma pressure in front of the target, leading to a reduced heat load compared to the pure H_2 seeding case. An opposite trend has been found concerning He and Ar puffing. In fact, injection of H_2 + He and H_2 + Ar gas mixtures led to an increased heat flux. To address the importance of different plasma-chemical reaction paths, global plasma models have been used. The resulting reduced reaction schemes for Ar + H_2, He + H_2, and $N_2 + H_2$ have been implemented in B2.5-Eunomia, a coupled code consisting of a Monte Carlo code treating the transport of neutrals and a fluid code solving plasma equations. Simulation results qualitatively reproduce the favorable effect of N_2, while confirming the deteriorating effect of He and Ar on a detachedlike hydrogen plasma. We point the synergetic role of $H_2 + N_2$ to be due to molecular-driven ion recombination, i.e., N-molecular-assisted recombination (MAR). A direct comparison of the collision frequency between N-MAR and MAR is showed, highlighting the crucial importance of the former in reducing the ion and heat flux to the target plate.

I. INTRODUCTION

Understanding how to limit and control the enormous heat and particle flux foreseen to be deposited on the divertor plates of future nuclear fusion reactors, e.g., ITER, is one of the most crucial issues to be solved in order to achieve fusion electricity.[1] The plasma ejected from the core is channeled along the Scrape-Off-Layer (SOL) toward the plasma-facing-components (PFC)[2] located in the divertor region.[3] Divertor plasma parameters in ITER are expected to be $n_e > 10^{20}$ m^{-3} with $T_e < 5$ eV, leading to head loads of about 10 MW m^{-2} for steady state operation and up to a few gigawatts per meter square during intrinsic instabilities of the core such as edge-localized-modes (ELMs).[4] Power is conveyed to the PFC via the ion potential energy, kinetic energy of electrons, ions, and neutrals, and via radiated power.[5] To make such heat flux tolerable, the so-called detached plasma regime has to be achieved.[6] Detachment is characterized by a plasma pressure reduction along magnetic field lines in the direction of the divertor target; such a drop is due to momentum transfer by means of electron/ion elastic collisions with neutrals and charge exchange, plasma radiation, and volume recombination. The heat flux to the target, q_w, can be expressed as

$$q_w = \Gamma\,(\gamma k_b T_e + E_i)\,[\mathrm{Wm} - 2\mathrm{s} - 1], \tag{1}$$

where Γ is the particle flux, γ is the sheath heat transmission coefficient, T_e is the electron temperature, and E_i is the ion potential.[7] The sole plasma cooling is not enough to minimize the power load to tolerable values; hence, reducing the particle flux to the target is necessary. In hydrogen plasma scenarios, this occurs by means of electron-ion recombination processes (EIR) and molecular-assisted recombination (MAR), both producing electronically excited states whose energy will be released in the form of photons. These processes are

$$H^+ + e^- + e^- \rightarrow H^*(n \geq 6) + e^-, \quad \text{EIR},$$
$$H^+ + H_2(v) \rightarrow H_2^+ + H, \quad \text{MAR (step 1)},$$
$$H_2^+ + e^- \rightarrow H + H^*(n = 2 - 4), \quad \text{MAR (step 2)}.$$

In such a way, ions are converted to neutrals before reaching the target, thus avoiding the release of the potential and kinetic energy onto

the plate[8] and preventing erosion of PFC. In divertor plasma detachment, volumetric processes play a key role in extinguishing charged particles, eventually reducing the heat flux.[9,10] In this paper, the importance of hydrogenic volume recombination is compared to impurity-driven recombination processes. In particular, light is shed on the mechanisms leading to the neutralization of hydrogen plasma induced by impurity-driven reactions (Sec. IV).

Experiments in tokamaks since the mid-1990s have demonstrated steady-state detached regimes by puffing neutral gas in the divertor region,[11] observing the recombination front moving upward from the PFC.[12] Furthermore, seeding of the so-called impurities in the tokamak mid-plane and/or in the divertor region facilitates the achievement of detachment.[13] Nitrogen is currently the leading candidate for impurity seeding in ITER,[14] given its radiative capabilities. Other species, such as argon and helium, have been studied as potential impurities for detachment and plasma cooling purposes.[15] Little is known about the effect on recombination mechanisms and plasma parameters that these species may cause once injected into such high-density low-temperature divertor-relevant hydrogen plasma.

Linear machines, sometimes referred to as divertor simulators, have actively contributed to a deeper understanding of detachment and plasma-edge physics. The great diagnostics accessibility, together with the capability of sustaining a long steady-state pulse and the relatively low cost of operation,[16] makes linear machines a fruitful tool to study plasma-neutrals interactions occurring during impurity seeding in detail.

In this work, we investigate the influence of three different impurities, N_2, He, and Ar, together with H_2, in the target chamber of the recently upgraded linear machine Magnum-PSI. A description of the apparatus and the diagnostics that have been used is presented in Sec. II. To underline the most relevant plasma chemistry in such scenarios, global plasma models have been set up and will be presented in Sec. V. The most relevant plasma processes highlighted with global modeling have been implemented in a spatially resolved coupled code, i.e., Eunomia, a 3D Monte Carlo code simulating the transport of neutrals in linear machines and B2.5, a spatially resolved multifluid code that solves plasma equations. The aim is to study the behavior of different species and their influence on plasma detachment with both experimental observations and dedicated numerical simulations. The modeling pursued in this work with B2.5-Eunomia has to be considered as a "code experiment," rather than a quantitative benchmarking with experimental data. The scope is to highlight new relevant volumetric mechanisms occurring in a detachedlike hydrogen plasma. In fact, the inclusion of the plasma chemistry induced by the presence of impurities in-state-of-the-art codes is a necessary step toward a full description and understanding of the physics governing divertor plasmas during detachment operation. Although beyond the scope of this work, to carry out quantitative comparisons, dedicated studies on the free-parameters, i.e., cross field transport coefficients, potential boundaries, and plasma flow from the source might be needed. Moreover, the implementation of a certain class of reactions including $N_2(v)$ as a reactant would improve the accuracy of the overall analysis [to the knowledge of the authors, no scaling laws regarding the interaction between $N_2(v)$ and hydrogen plasma species have ever been published].

II. EXPERIMENTAL SETUP AND DIAGNOSTICS

Magnum-PSI is a linear plasma generator built to mimic the plasma-surface-interactions (PSI) that will occur in the ITER divertor. The machine can achieve plasma parameters of $T_e \leq 5$ eV and $n_e \geq 10^{19}$ m^{-3} with ion flux up to 10^{25} m^{-2} s^{-1}.[17] Those conditions lead to heat loads to the target of ~10 MW m^{-2}, i.e., the expected steady-state loads onto the ITER divertor plates.[18] By using a pulsed source, ELM-like heat loads up to few gigawatt per meter square can also be achieved.[19] In this work, only steady-state scenarios have been studied, both experimentally and by modeling. Magnum-PSI is characterized by three differentially pumped chambers, i.e., source and middle and target chamber, as can be seen in Fig. 1.

The plasma is generated by a cascaded arc source[20] and is confined by applying a magnetic field generated by a superconducting magnet. The beam travels through the three chambers and eventually reaches the target plate. Differential pumping between all three chambers is applied in order to minimize the presence of neutrals along the beam path, which would cause a cooling of the plasma and higher recombination, resulting in lower electron density. The target used in the experiments presented in this work consists of a tungsten circular target with a diameter of 3 cm and a thickness of 1 mm. A more detailed description of the machine can be found in Ref. 21.

Plasma parameters (temperature and density) have been diagnosed using a Thomson Scattering (TS) system[22] measuring at 3 cm in front of the target. A hydrogen plasma beam has been adopted for all the scenarios examined in this paper.

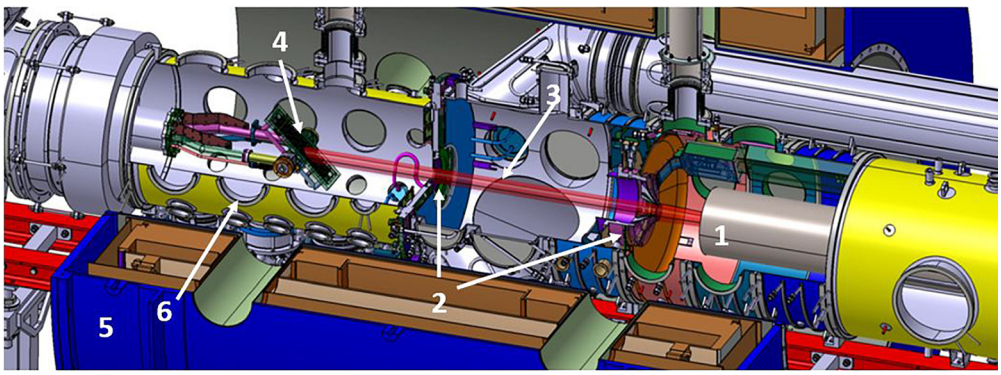

FIG. 1. Design of linear plasma machine Magnum-PSI. The numbers correspond to: 1, Plasma source, 2, Skimmers separating the three chambers, 3, Plasma beam, 4, Target, 5, Superconducting magnet, and 6, Impurity gas introduction location.

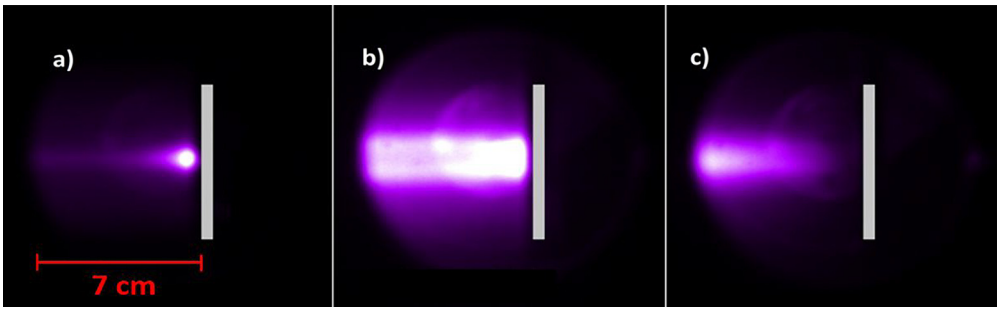

FIG. 2. Background neutral pressure scan on a hydrogen plasma beam facing the target. (a) Pressure = 0.3 Pa; (b) = 4.4 Pa; (c) = 16.8 Pa. The gray part represents the target location.

To study plasma radiation during H_2 and N_2 seeding in detachment experiments, a resistive bolometer has been used. More details on this diagnostic can be found in Ref. 23. The gas seeding valve, necessary for plasma detachment studies, is located laterally in the target chamber just behind the target. To measure the background neutral pressure in the chamber, a baratron type MKS 627B is used. It is located further behind the target compared to the seeding valve.

A two-channel fiber optic spectrometer (AvaSpec-ULS2048) has been used during nitrogen seeding experiments to observe the line intensity at 336 nm. Such wavelength corresponds to the $NH^*(A^3\Pi->X^3\Sigma^-)$ electronic transition. That species is of great interest in our work, concerning both experiments and simulations. The OES (Optical Emission Spectroscopy) view is located at the same axial coordinates as TS, i.e., 3 cm in front of the target. To study the heat and particle flux deposited to the tungsten target, calorimetry has been used.

III. PLASMA DETACHMENT WITH HYDROGEN SEEDING

Plasma detachment has been successfully achieved in Magnum-PSI by increasing the background neutral pressure in the target chamber by actively seeding hydrogen gas. In Fig. 2, three snapshots taken during a background pressure scan are shown. Hydrogen plasma has been used. Images are taken with a phantom camera V12.1. A balmer-α filter has been applied. The target is a tungsten disk with 3 cm diameter and 1 mm thick.

Figure 2(a) shows a typical high-recycling regime, where ions recombine on the target and are re-emitted as ground state molecules in vibrational excitation or atoms. Those particles will be soon excited via electron-impact in the vicinity of the surface, given the short mean-free-path. Plasma parameters in such conditions were $T_e = 3.94$ eV and $n_e = 1.11 \times 10^{20}$ m^{-3} and the background neutral pressure was 0.3 Pa. A recombining plasma is observed in Fig. 2(b); in such a case, plasma parameters were $T_e = 0.8$ eV and $n_e = 2.4 \times 10^{20}$ m^{-3} with a pressure of 4.4 Pa. In these conditions, recombination of ions occurs extensively ($T_e < 2$ eV and $n_e > 10^{20}$ m^{-3}). More specifically, MAR and three-body recombination, i.e., $H^+ + e^- + e^- \rightarrow H^*(n > 5) + e^-$ are the main processes leading to the observed emission throughout the beam[24] together with the broadening of the emission. To unequivocally define the relative contribution of MAR and EIR on the scenario shown in Fig. 3(b), a dedicated CR (Collisional Radiative) model should be set up. This goes beyond the scope of this paper. Nevertheless, Balmer-α emission is mostly due to MAR processes, which are initiated by molecular hydrogen in the vibrational excited state. In fact, one can observe a hollowness in the emitted light from the plasma beam up to few cm in front of the target. Such an effect is due to $H_{2(v>4)}$ molecules coming

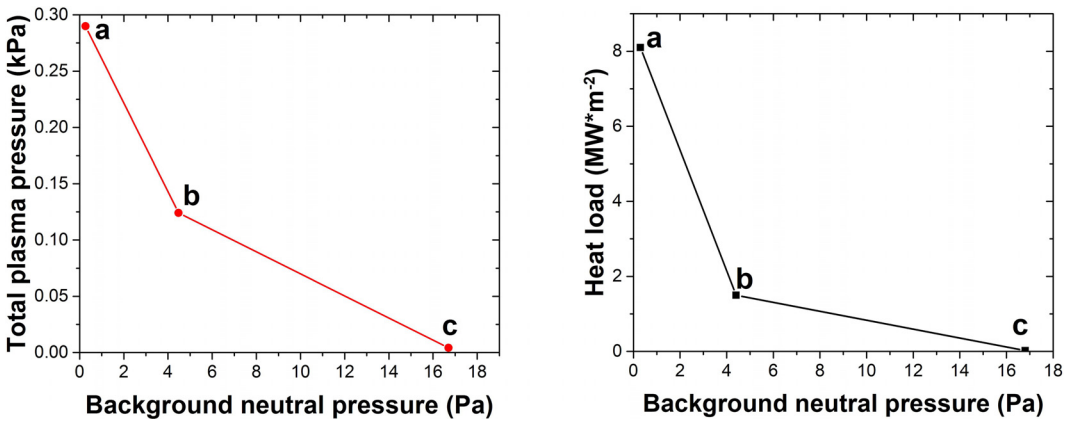

FIG. 3. (Left). Total plasma pressure as a function of background neutral pressure in the target chamber of Magnum-PSI. At a neutral pressure of 0.3 Pa, plasma pressure is about 0.29 kPa (point a). It goes down to 0.12 kPa at 4.4 Pa (point b) and eventually falls to 0.0042 kPa at 16.8 Pa (point c). (Right) Heat load to the target, calculated with Eq. (1), for the same background neutral pressures of Figs. 2 and 3 (left).

from the side of the plasma beam that eventually undergo through MAR. The brightness in front of the target is due to $H_{2(v>4)}$ coming from the wall and undergoing the same process. The mean-free-path of those species is longer compared to Fig. 2(a) because of the milder conditions of the plasma ($T_e < 1$ eV). Figure 2(c) depicts an almost entirely extinguished plasma: neutral pressure was 16.8 Pa and led to parameters to be $T_e = 0.16$ eV and $n_e = 4 \times 10^{19}$ m^{-3}. It is hereby proved that different degrees of detachment can be achieved by means of Magnum-PSI. To further characterize the above-mentioned three cases of study, total peaked static plasma pressure (dynamic ion pressure is not included) has been calculated assuming a quasineutral thermal plasma, i.e., $P_p = 2kT_e n_e$. Results are shown in Fig. 3.

Points (a), (b), and (c) in Fig. 3 (left and right) correspond to the same ones depicted in Fig. 2. The total plasma pressure, derived by Thomson scattering measurements, steeply decreases while enhancing the neutral background pressure by H_2 gas puffing in the target chamber. It goes from $P_{plasma} \approx 0.29$ kPa at $P_{neutrals} = 0.3$ Pa (point a), to $P_{plasma} = 0.12$ kPa at 4.4 Pa (point b) and eventually to $P_{plasma} = 0.0042$ kPa at $P_{neutrals} = 16.8$ Pa (point c). At the highest background neutral pressure, plasma is almost entirely recombined before reaching the watts target. Steady-state plasma detachment is achieved in Magnum-PSI by impurity seeding. Experiments regarding how different impurities injected together with H_2 at different mixture ratios influence plasma detachment in ITER-divertor relevant conditions are presented and discussed in Sec. IV.

IV. PLASMA DETACHMENT WITH IMPURITY SEEDING (N_2, Ar, AND He)

A comparative study among different impurity species and their effect on plasma detachment has been carried out. Impurities have been seeded, together with H_2, with different mixing ratios defined by the partial pressure; the background neutral pressure in the target chamber has been kept constant at 2 and 4 Pa, while changing the ratio as

$$\frac{[impurity]}{[H_2] + [impurity]} * 100 = 0\%,\ 5\%,\ 10\%,\ 15\%,\ 20\%.$$

Three different gas species have been puffed with hydrogen, i.e., nitrogen, helium, and argon. The last two species are poorly reactive, while N_2 and related compounds such as NH_3, NH_2, and NH react with species populating the generated hydrogen plasma, e.g., H^+, H_2^+, H, and $H_2(v)$.[25] In this section, we study experimentally the influence of different impurity seeding on plasma parameters by means of the plasma pressure and the heat flux collected at the target. The injected gas mixtures are $H_2 + N_2$, H_2 + He, and H_2 + Ar, and the plasma pressure, calculated with Thomson scattering, is shown in Fig. 4. These measurements have been taken in the plasma volume, at 3 cm in front of the tungsten target.

For the scans of both background pressures, the baseline scenario, i.e., with only H_2 puffing, corresponds to the first point, i.e., when no impurity was added into the mixture. Although each baseline scenario can be slightly different due to limited reproducibility of the machine, every scan is carried out maintaining the same experimental conditions among each other. At 2 Pa with N_2 seeding up to 20%, we observe a clear decay that leads to a plasma pressure loss of ≈25%. In the helium case, a different trend is achieved. Here, the plasma pressure somewhat varies around 0.21 kPa and remains almost constant. Regarding the Ar-seeding case, the behavior is similar to the helium one: after a small decrease at 5%, P_{plasma} increases by about 10% during the scans at 10%, 15%, and 20% of impurity content, hence reducing the effectiveness of detachment. If on the one hand the addition of a mixture of H_2/N_2 is beneficial for plasma detachment compared to H_2 puffing alone, the other two species show an opposite effect, enhancing the plasma pressure in front of the target.

To unequivocally investigate the effect of these impurities on plasma recombination, heat fluxes collected at the target have been diagnosed by means of calorimetry and results are reported in Fig. 5. The power deposited to the tungsten disk is calculated as $P(W) = flow\left(\frac{kg}{s}\right) dT(K) 4200\left(\frac{J}{kg\,K}\right)$, with $flow = 0.4\frac{kg}{s}$ being the amount of cooling water passing through the diagnostic per second, dT the water temperature difference before and after it has been passed through the heated component, and 4200 J is the energy needed to heat up 1 l of water by 1 K. It is worth stressing that for the calculation of the heat flux no direct measurements of plasma parameters are used; in such a way we can straightforwardly measure the actual heat transported by the plasma to the target. The power load at the target is mostly due to surface recombination of incoming hydrogen ions, where they release

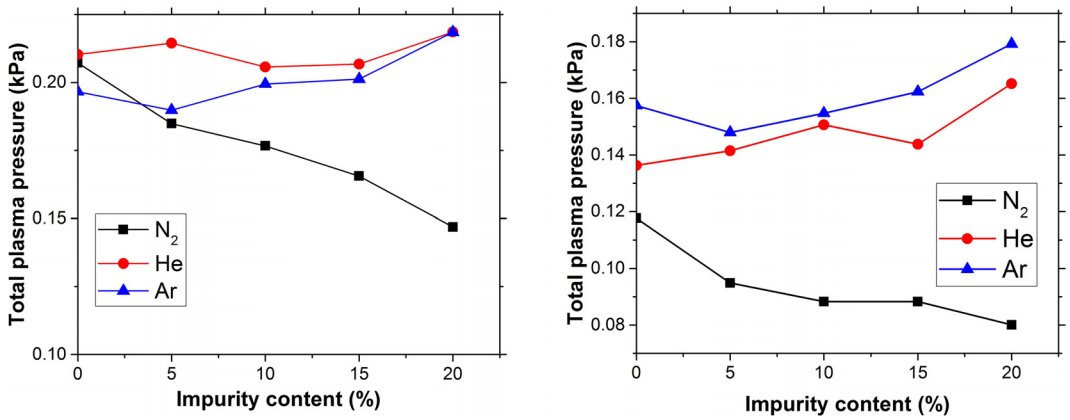

FIG. 4. Total plasma pressure as a function of impurity content for N_2, He, and Ar. The neutral background pressure in the target vessel is constant at 2 Pa (left) and 4 Pa (right).

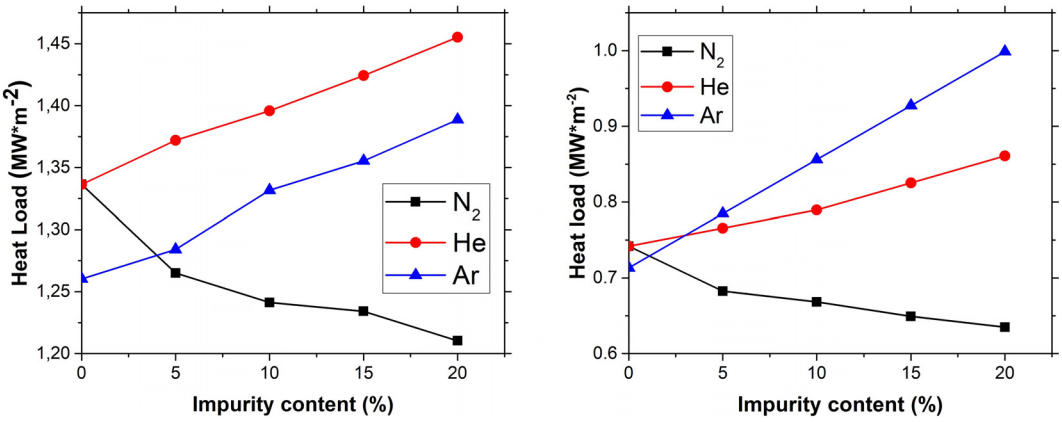

FIG. 5. Heat load on the W target for each impurity at different H_2/impurity mixing ratios at 2 Pa (left) and 4 Pa (right).

their potential and (part of their) kinetic energy, which causes heating of the material. In Fig. 5 (left), the starting value of heat load for the Ar seeding scan, i.e., Ar = 0% is lower compared to H_2/N_2 and H_2/He cases by $\approx$ 0.7 MW m^{-2}. Although the experimental settings have been kept the same, plasma conditions were not perfectly reproducible. Nevertheless, for the scope of this work, the trend obtained by puffing different ratios of different species is the most relevant feature to be highlighted and studied.

At a background neutral pressure of 2 Pa, when H_2 is diluted with He, the measured heat load increases by ≈11%, from 0% to 20% of impurity content. Regarding N_2, we obtain a net reduction of heat flux of about 12%. Such findings further confirm the beneficial effect for detachment led by the presence of N_2 in the seeded gas mixture. Argon puffing experiments are characterized by an enhancement of heat deposited to the surface of ≈12%, implying a reduced detachment efficiency.

The same experiments have been carried out with a fixed background pressure of 4 Pa and results are plotted in Figs. 4 (right) and 5 (right). The same behavior is observed compared to the 2 Pa case; in fact, P_{plasma} increases by ≈15% between 0% and 20% of impurity content, for both He and Ar. H_2/N_2 puffing led to a plasma pressure reduction of ≈28%. The heat flux is reduced by the presence of N_2 by 18%, while it is enhanced by 16% and almost 40% with H_2/He and H_2/Ar, respectively.

According to these results, Ar seems to be the less beneficial species among the impurities exploited in this study. Helium shows a negative impact on plasma detachment as well, while nitrogen led to an improved detached state among both 2 and 4 Pa cases. Three different impurities have been tested in ITER-relevant hydrogen plasma at the same experimental conditions for the first time. The negative outcome on plasma pressure and heat flux of Ar and He seeding may be due to the dilution effect, i.e., fewer hydrogen molecules are inserted in the system; therefore, less molecule-driven ion recombination occurs in the volume phase. This is not the case for N_2, which shows an effective improvement in the detached plasma performance. When mixtures of $H_2 + N_2$ are injected into the vessel, the heat flux is subjected to a net decrease. This behavior is appointed by the authors to be due to the presence of N_2-driven ion recombination processes, as discussed in Ref. 26. The role of NH_x molecules, i.e., NH_3, NH_2, and NH as electron donors in the reaction with H^+ has been found to be of great importance in divertor-relevant hydrogen plasma. Specifically, the following two-step process was found by numerical simulations to be relevant:

(1) $H^+ + NH_x \rightarrow H + NH_x^+$
(2) $NH_x^+ + e^- \rightarrow NH_{x-1} + H.$

Such a mechanism is referred to as N-MAR,[27] and is characterized by an ion conversion promptly followed by dissociative recombination. This process effectively converts ion to neutral, thus dissipating energy from the plasma via volumetric recombination. This may result in a reduced heat flux when increasing the $H_2 + N_2$ puffing ratio. To investigate the presence of N_2-H_2 species in the plasma, optical-emission-spectroscopy has been adopted and the outcome is shown in Fig. 6.

On the left, the identification of the main peaks diagnosed with OES is shown. Balmer lines, in particular the transitions $n = 5 \rightarrow n = 2$ (*Balmer* γ) and $n = 6 \rightarrow n = 2$ (*Balmer* δ) at 434 nm and 410 nm respectively, are shown. N_2 transition $C^3\Pi$->$B^3\Pi$ at 338 nm is also present. Of particular interest is the peak at 336 nm, which is due to the $NH^*(A^3\Pi->X^3\Sigma)$ transition, the NH radical being the electron donor in the N-MAR first step, i.e., ion conversion with H^+ in high density plasmas. On the right, the intensity of the 336 nm band is plotted as a function of N_2 content in the puffed $H_2 + N_2$ mixture and calculated as $\int \frac{I(\lambda)}{t(exposure)} d\lambda$. The achieved trend clearly indicates a relevant presence of such species in the plasma, thus providing a further indication on the enhanced recombination of hydrogen ions led by NH_x species. To study the radiated power emitted during the seeding scan, a bolometry system has been used. By such a diagnostic, we can include/exclude cooling phenomena led by relaxation of electronically excited species. Results are shown in Fig. 7.

The total radiated power, averaged over the 3 viewing channels, is calculated as

$$P_{rad} = \frac{\pi^2 l_{s,ap}^2}{A_s A_{ap}} d_p \Delta z P_s, \quad (2)$$

where $l_{s,ap}$ is the distance between the sensor and the aperture, A_s is the sensor area, A_{ap} is the aperture area, d_p is the plasma diameter taken as the FWHM measured by Thomson scattering, Δz is the axial width, and P_s is the power received by the sensor of a bolometer

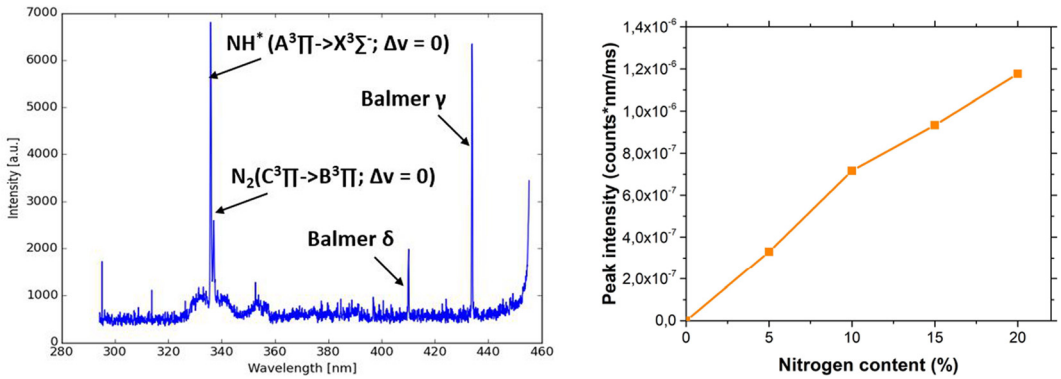

FIG. 6. (Left): Emission spectra for a H_2 plasma with H_2/N_2 seeding with peak identification. (Right): Peak intensity of the NH* band at 336 nm for a neutral background pressure of 2 Pa.

channel and is calculated as follows: $P_s(t) = \frac{1}{S}\left(\Delta U(t) + \tau \frac{d\Delta U(t)}{dt}\right)$,[23] where S is the sensitivity of the instrument. No substantial trend in plasma radiation is collected while increasing the content of nitrogen in the puffed gas mixture. Therefore, we shall exclude the power-limitation effect[28] (often referred to as "power starvation") that would lead to a drop in plasma pressure, basically shifting the recombination front backward from the target. The fact that no trend is observed with bolometry further suggests that the reduced heat flux and plasma pressure drop shown in Figs. 4 and 5 may be due to volume recombination processes occurring before ions reach the target.

Dedicated experiments in linear plasma machines GAMMA10/PDX[29] and PISCES-E[30] showed similar trends to the ones presented here, i.e., a synergetic effect of $H_2 + N_2$ seeding in the recombination of hydrogen ions is observed in both cases. Plasma parameters differ substantially, with T_e around 10 eV and $n_e \approx 10^{17}$ m^{-3} in GAMMA10/PDX and T_e of about 2 eV with $4 \times 10^{16} < n_e < 3 \times 10^{17}$ m^{-3} in PISCES. Nevertheless, combining those works with this one, the effect of impurities over a wide parameter space can be studied.

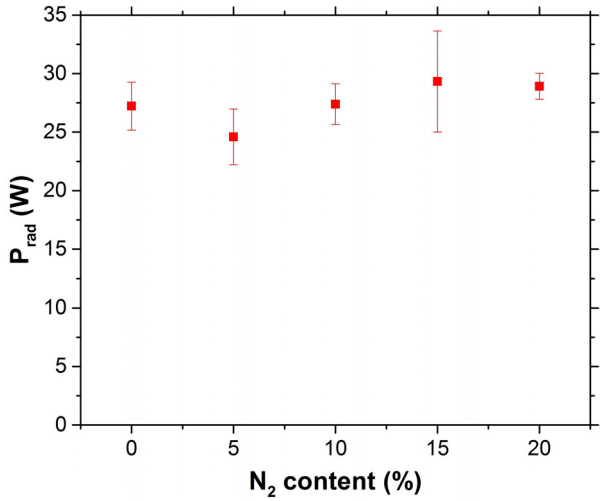

FIG. 7. Plasma radiation during the H_2-N_2 seeding scan.

In order to shed more light into the physics and the chemistry that are governing these scenarios, numerical simulations are needed. To do so, a two-step approach has been followed and details are provided in Secs. V and VI. First, volume-averaged plasma models have been setup with the aim of highlighting the most relevant plasma chemical reactions. Subsequently, these processes have been implemented in the B2.5-Eunomia coupled code. These methods are described in Secs. V and VI.

V. GLOBAL MODEL

Global models are zero-dimensional simulations that allow one to implement large plasma chemical data sets, given the assumption of a homogeneous distribution of species and plasma parameters throughout a defined volume.[31] The simulations have been set up using the Plasimo code.[32] The code solves a system of coupled differential equations: particle balance, quasineutrality, and energy balance. The adopted electron energy distribution function (EEDF) is Maxwellian. The electron energy balance is calculated as

$$\frac{d\left(\frac{3}{2} n_e e T_e\right)}{dt} = P_{input}(t) - Q_{coll} \tag{3}$$

with e the elementary charge, n_e and T_e electron density (per cubic meter) and temperature (electron volt), P_{input} the input power density, and Q_{coll} the energy losses via inelastic and elastic collisions. The time-evolution of both plasma and neutral species is calculated as follows:

$$\frac{dn_i}{dt} = \sum \left(s_i^p - s_i^r\right) k(t) \prod n_i^{s_r}, \tag{4}$$

where s_i^p and s_i^r are the stoichiometric coefficients of products and reactants, respectively, $k(t)$ is the reaction rate, and n_i is the density of the species i. The reaction rate coefficients are written in the generalized Arrhenius form

$$k(T_e) = A * \left(\frac{T_e}{1eV}\right)^n * \exp\left(-\frac{E_a}{T_e}\right), \tag{5}$$

where A is declared in cubic centimeter per second and E_a is the activation energy of the reaction, together with T_e, in electron volt. This types of codes are computationally cheaper than spatially resolved hybrid models; hence, we can implement extensive chemistry without

implying a significant increase in the computational effort.[33] A wide and detailed global model for $N_2 + H_2$ divertor relevant plasmas, together with a full description of the code, can be found in Ref. 27. Global models have been therefore used in this study for (1) providing theoretical insights into the results achieved during detachment experiments and (2) to highlight the most relevant volume processes to be implemented into a spatially resolved coupled code.

Regarding the H_2 + He seeding case, in Fig. 5 we observe an increase in roughly 10% of the power load with increasing the content of He in the puffed gases. Such a trend is believed to be indicative of less recombination, due to dilution of molecular hydrogen. The reactions involving helium and included in the model are listed in Table I. Given that the aim of this study is to understand the influence of different impurities on plasma recombination and detachment, particular attention has been given to the recombination paths of H^+ and H_2^+ in the presence of He. The rate for some of the electron-induced reactions is calculated by the code by integrating the cross section over a Maxwellian electron energy distribution function (EEDF), as follows:

$$k_r = \int_{E_t}^{\infty} \sigma_r(E)\, v(E) f(E)\, d(E), \tag{6}$$

where E_t is the threshold energy of the collision, E is the electron energy, $f(E)$ is the EEDF, $v(E)$ is the electron thermal velocity, and σ_r is the cross section of collision r. In the simulations, one vibrationally excited species for molecular hydrogen, namely, v = 4, and one electronically excited state for atomic helium (He^*2^3S) have been included. They are important for ion conversion [reaction (7)] and two-step ionization [reactions (10) and (12)], respectively.

No mechanisms involving directly H^+ and He have been found in the literature. Nevertheless, the proton transfer reaction [reaction (15)] between H_2^+ and He, followed by dissociative recombination, i.e., $HeH^+ + e^- \rightarrow He + H$ [reaction (14)], constitutes a further neutralization path. Numerical results indicate that, for electron density of $n_e \approx 1 \times 10^{19}$ m^{-3} the main molecule-driven route for H_2^+ consumption is with H_2, leading to the production of H_3^+. Reaction (15) is responsible for only 5% of the total sinks of H_2^+. With $n_e \approx 1 \times 10^{20}$ m^{-3}, the main sink is entirely via dissociative recombination [reaction (8)]. The electron temperature for those simulations was 1.5 eV. A schematic representation of these results is presented in Fig. 8.

The density distribution of molecular ions in a H_2 + He plasma calculated with the global model is plotted in Fig. 9. In the simulation, the initial densities of H_2 and He correspond to a 5% impurity seeding case, i.e., $n_{H2} = 1 \times 10^{21}$ m^{-3} and $n_{He} = 5 \times 10^{19}$ m^{-3}. The parameter that mostly influences the population of ions in such low temperature—high density plasmas is the electron density. In Fig. 9, the amount of ions (per cubic meter) has been calculated for n_e between 6×10^{18} and 1×10^{20} m^{-3}. With n_e below 10^{19} m^{-3}, the dominant species is H_3^+, which is produced via reaction (6). HeH^+ has a peak at $n_e \sim 2 \times 10^{19}$ m^{-3}, which also corresponds to the electron density where H^+ becomes basically as populated as H_3^+. When moving

TABLE I. Helium-driven plasma chemical reactions adopted in the H_2/He global model.

No.	Reaction	Rate (m^3 s^{-1})	References
1	$H_2 + e^- \rightarrow H + H + e^-$	From cross section	34
2	$H_2 + e^- \rightarrow H_2(v = 4) + e^-$	From cross section	35
3	$H_2 + e^- \rightarrow H^+ + H + 2e^-$	$9.4 \times 10^{-16} \times T_e^{0.45} \times \exp\left(-\frac{29.94}{T_e}\right)$	36
4	$H + e^- \rightarrow H^+ + 2e^-$	From cross section	37
5	$H_2 + e^- \rightarrow H_2^+ + 2e^-$	From cross section	38
6	$H_2^+ + H_2 \rightarrow H_3^+ + H$	2×10^{-15}	39
7	$H_2(v = 4) + H^+ \rightarrow H_2^+ + H$	2.5×10^{-15}	40
8	$H_2^+ + e^- \rightarrow H + H$	$1.6 \times 10^{-14} \times T_e^{-0.43}$	41
9	$H_3^+ + e^- \rightarrow H_2 + H$	$4.36 \times 10^{-14} \times T_e^{-0.52}$	42
10	$He + e^- \rightarrow He^*(2^3S) + e^-$	$5.05 \times 10^{-14} \times \exp\left(-\frac{22.5}{T_e}\right)$	43
11	$He^*(2^3S) \rightarrow He + h\nu$	6.72×10^{11}	43
12	$He^*(2^3S) + e^- \rightarrow He^+ + 2e^-$	$1.28 \times 10^{-13} \times T_e^{0.6} \times \exp\left(-\frac{4.78}{T_e}\right)$	43
13	$He + e^- \rightarrow He^+ + 2e^-$	$1.5 \times 10^{-15} \times T_e^{0.68} \times \exp\left(-\frac{24.6}{T_e}\right)$	43
14	$HeH^+ + e^- \rightarrow He + H$	$1.0 \times 10^{-14} \times T_e^{-0.6}$	41
15	$H_2^+ + He \rightarrow HeH^+ + H$	1.3×10^{-16}	39
16	$He^+ + H_2 \rightarrow He + H_2^+$	1.7×10^{-21}	39
17	$HeH^+ + H \rightarrow He + H_2^+$	9.1×10^{-16}	39
18	$HeH^+ + H_2 \rightarrow He + H_3^+$	1.8×10^{-15}	39
19	$He + e^- \rightarrow He + e^-$	From cross seciton	44

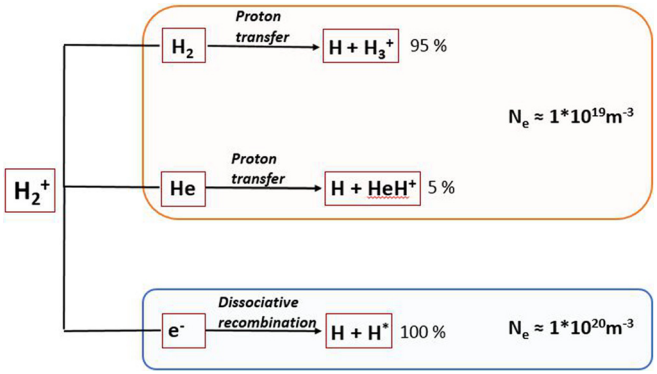

FIG. 8. Global model output of H_2^+ sink reaction paths in a H_2/He plasma for two electron density scenarios. T_e was 1.5 eV in both cases.

toward higher n_e, dissociative recombination of H_2^+ becomes very efficient, hence a depopulation of such molecule occurs (H_2^+ is the precursor of H_3^+). As a result, for divertor-relevant and Magnum-PSI typical plasmas, no additional recombination effects are driven by the presence of He.

Although no beneficial effects for detachment come along the presence of He, as it is shown experimentally and confirmed hereby by the global model, a spatially resolved code is mandatory to exclude/include any further mechanism that could influence plasma parameters in a detachedlike scenario, such as elastic processes leading to momentum loss and/or influences on the radial transport. These simulations will be presented in Sec. VI D.

Concerning the Ar seeding cases depicted in Fig. 4, a similar behavior to the one with H_2 + He puffing is measured. In fact, the more argon is injected into the system, the more heat is deposited on the W target. The power load increases by ≈10% between the 0% Ar and the 20% Ar in the seeded mixture. This phenomenon is appointed to be again due to dilution of hydrogen molecules, reflecting in less

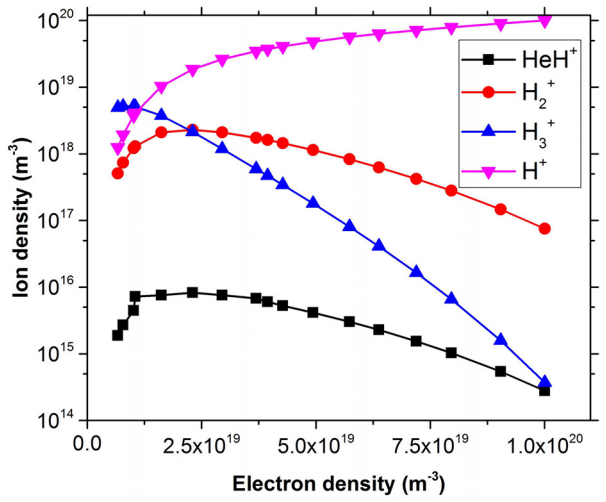

FIG. 9. Density of molecular ions as a function of n_e calculated with PLASIMO.

volume recombination of the plasma, hence lowering the dissipation of ion potential before reaching the plate. In order to closely look into volume processes occurring in a hydrogen plasma with H_2 + Ar seeding, another global plasma model has been created. Hydrogen-related processes are identical to the ones in Table I. An electronically excited state of Ar, i.e., Ar^*4p, has been added being an important intermediate state for multistep ionization. Reactions are reported in Table II.

Concerning H_2^+, for low n_e, proton transfer with H_2 and that with Ar are the main sinks and account for 85% and 15% respectively, producing H_3^+ and ArH^+. For Magnum-PSI-relevant plasma conditions, where n_e is on the order of $1–5 \times 10^{20}$ m^{-3}, H_2^+ is consumed almost entirely by dissociative recombination, while proton transfer [reaction (16)] constitutes only 5% of the total sink processes. For electron densities $\approx 1 \times 10^{19}$ m^{-3}, the sources for H_3^+ are proton transfer reactions, i.e., reactions (6) and (17). The contributions are about 80% and 20%, respectively. Above such a density threshold, H_3^+ is barely produced due to the very efficient dissociative recombination of its precursor H_2^+ [reaction (8)]. The main sink for H_3^+ is reaction (9) in both cases. The electron temperature is set at 1.5 eV. Argon appears to have a similar behavior to helium, in these experimental conditions. A visual representation of these plasma chemical paths is reported in Fig. 10.

It has been shown that no ion-recombination paths appear to be relevant in the presence of either Ar and He among the parameter range considered in this study. In the case of N_2, however, the outcome is different. In fact, N-H induced volume-recombination processes seem to play a crucial role in divertor-relevant detachedlike hydrogen plasma. To further study those findings, B2.5-Eunomia simulations have been carried out, aiming to provide insights into the effect of two different impurities, i.e., He and N_2 on plasma detachment in Magnum-PSI.

VI. EUNOMIA CODE

Eunomia is a 3D Monte Carlo code developed to model the neutral transport in linear plasma machines.[47] It is conceptually very similar to the well-established code EIRENE.[48] The code has been originally created to study neutrals in Pilot-PSI,[49] the predecessor of Magnum-PSI. For this work, a new grid with Magnum-PSI geometry has been created and will be shown in Sec. VI A. In the code, the so-called test particles are traced: they are representative of many neutral particles. Such way of treating species is called test particle approximation method. In Eunomia standalone, the plasma equations are not solved; the plasma background is assumed to be constant and has to be provided as input. When a test particle collides with a charged or neutral particle from the background, the information regarding the obtained products and velocity distribution are stored by the code for every cycle. The new background is then updated at the beginning of the next cycle. The number of particles per cell is calculated by the code as

$$N_p = \Gamma_p T_a \tag{7}$$

with Γ_p the influx of particles into the system (per second) and T_a the residence time (averaged). The Boltzmann transport equation, which describes the statistical behavior of a gas or fluid, is solved by Eunomia as

$$\mathbf{v} \cdot \nabla_{\mathbf{r}} f(\mathbf{r}, \mathbf{v}, i) = \sum C(\mathbf{r}, \mathbf{v}, i, j) + S(\mathbf{r}, \mathbf{v}, i), \tag{8}$$

TABLE II. Argon-driven plasma chemical reactions adopted in the H_2/Ar global model. Hydrogenic reactions adopted are the ones listed in Table I.

No.	Reaction	Rate ($m^3\ s^{-1}$)	References
1	$H_2 + e^- \rightarrow H + H + e^-$	From cross section	34
2	$H_2 + e^- \rightarrow H_2(v = 4) + e^-$	From cross section	35
3	$H_2 + e^- \rightarrow H^+ + H + 2e^-$	$9.4 \times 10^{-16} \times T_e^{0.45} \times \exp\left(-\frac{29.94}{T_e}\right)$	36
4	$H + e^- \rightarrow H^+ + 2e^-$	From cross section	37
5	$H_2 + e^- \rightarrow H_2^+ + 2e^-$	From cross section	38
6	$H_2^+ + H_2 \rightarrow H_3^+ + H$	2×10^{-15}	39
7	$H_2(v = 4) + H^+ \rightarrow H_2^+ + H$	2.5×10^{-15}	40
8	$H_2^+ + e^- \rightarrow H + H$	$1.6 \times 10^{-14} \times T_e^{-0.43}$	41
9	$H_3^+ + e^- \rightarrow H_2 + H$	$4.36 \times 10^{-14} \times T_e^{-0.52}$	42
10	$Ar + e^- \rightarrow Ar^+ + 2e^-$	$2.39 \times 10^{-14} \times T_e^{0.57} \times \exp\left(-\frac{17.43}{T_e}\right)$	45
11	$Ar^*(4p) + e^- \rightarrow Ar^+ + 2e^-$	$1.23 \times 10^{-12} \times T_e^{0.25} \times \exp\left(-\frac{3.71}{T_e}\right)$	45
12	$Ar^+ + H_2 \rightarrow Ar + H_2^+$	2×10^{-17}	39
13	$Ar^+ + H_2 \rightarrow ArH^+ + H$	6.7×10^{-16}	39
14	$Ar + H_3^+ \rightarrow ArH^+ + H_2$	3.7×10^{-16}	39
15	$Ar + H_2^+ \rightarrow Ar^+ + H_2$	2×10^{-16}	39
16	$Ar + H_2^+ \rightarrow ArH^+ + H$	2.1×10^{-15}	39
17	$ArH^+ + H_2 \rightarrow H_3^+ + Ar$	6.3×10^{-16}	39
18	$ArH^+ + e^- \rightarrow Ar + H$	1×10^{-15}	46
19	$Ar + e^- \rightarrow Ar + e^-$	From cross section	44

where the left-hand side is the velocity vector times the probability density function (f) of species i in position $\mathbf{r}$ and velocity $\mathbf{v}$, $\sum C(\mathbf{r}, \mathbf{v}, i, j)$ is the collision term of inelastic and elastic collisions between neutrals and plasma particles and $S(\mathbf{r}, \mathbf{v}, i)$ is the source term. Eunomia incorporates particle sources and sinks, i.e., absorption due to pumping, conversion of ions to neutrals, recycling, and gas puffing. For a more detailed overview on the theoretical background of Eunomia, the reader is referred to Ref. 50. The hydrogenic plasma chemistry contained in Eunomia is shown in Table III.

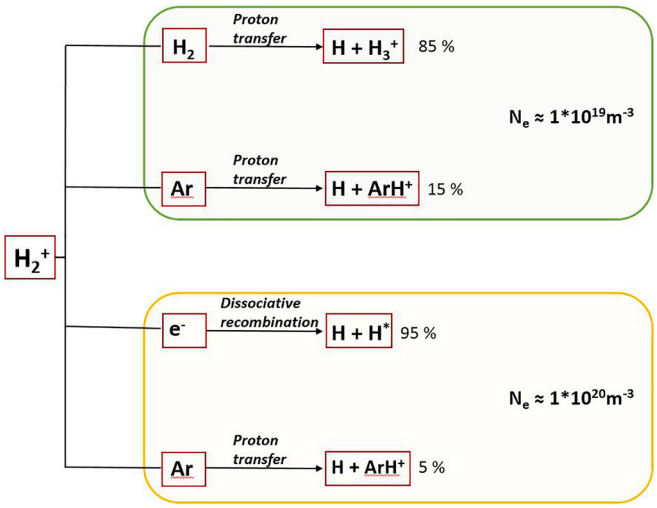

FIG. 10. Global model output of H_2^+ sink reaction paths in a H_2/Ar plasma for two electron density scenarios. T_e was 1.5 eV in both cases.

TABLE III. Hydrogen plasma chemistry included in Eunomia and suited for studying standard H_2 plasma operations.

No.	Reaction	Type
1	$H + H \rightarrow H + H$	Elastic collision
2	$H + H_2 \rightarrow H + H_2$	Elastic collision
3	$H_2 + H_2 \rightarrow H_2 + H_2$	Elastic collision
4	$H + e^- \rightarrow H^+ + 2e^-$	Ionization
5	$H^+ + H \rightarrow H + H^+$	Charge exchange
6	$H_2 + e^- \rightarrow H + H + e^-$	Dissociation
7	$H_2(v) + e^- \rightarrow H_2(v \pm 1) + e^-$	Vibrational (de-)excitation
8	$H_2(v) + H^+ \rightarrow H + H_2^+$	Ion conversion
	$e^- + H_2^+ \rightarrow H + H_{n=2}^*$	Dissociative recombination (MAR)
9	$H_2 + e^- \rightarrow H + H^-$	Ion conversion
	$H^+ + H^- \rightarrow H + H_{n=3}^*$	Dissociative recombination (MAR)
10	$H + H^+ \rightarrow H + H^+$	Ion-neutral elastic collision
11	$H_2 + H^+ \rightarrow H_2 + H^+$	Ion-neutral elastic collision

A. Coupling B2.5-EUNOMIA

The scope of this paper is to study the effect on plasma detachment led by puffing different gas species, namely, $H_2 + N_2$ and $H_2 + He$, in the target chamber. New plasma chemistry has been implemented in the code, in order to study the differences between seeding a highly reactive species (nitrogen and ammonia-related compounds) with a poorly reactive one (helium).

To provide a full description of the Magnum-PSI scenario during detachment experimental campaigns, the spatially resolved kinetic Monte Carlo code Eunomia has been coupled with the multifluid code B2.5.[50] A detailed description of the code can be found in Ref. 51. The equations solved by the program are based on the Braginskii equations that are fully explained in Ref. 52. In brief, the code solves the continuity equation for ion i which is

$$\frac{dn_i}{dt} + \nabla \cdot (n_i v_i) = S_{ni} \tag{9}$$

with the parallel momentum equation being

$$\frac{d}{dt}(m_i n_i v_{i\parallel}) + \nabla \cdot (m_i n_i \mathbf{v}_i v_{i\parallel}) = -\nabla_\parallel p_i - (\nabla \Pi_i)_\parallel + Z_i e n_i \nabla_\parallel \phi + F_k + R_{i\parallel} + S_{m_i v_{i\parallel}}, \tag{10}$$

where $-\nabla_\parallel p_i$ is the ion pressure gradient, F_k is the Coriolis force, $\nabla \Pi_i$ is the viscosity tensor, $Z_i e n_i \nabla_\parallel \phi$ is the electric force, $R_{i\parallel}$ is the ion-electron friction, and $S_{m_i v_{i\parallel}}$ the ion-neutral friction. The parallel momentum balance for electrons is expressed as

$$j_\parallel = \sigma_\parallel \left(\frac{1}{en} \nabla_\parallel n T_e + \frac{0.71}{e} \nabla_\parallel T_e - \nabla_\parallel \phi \right) \tag{11}$$

with $\sigma_\parallel$ the parallel conductivity, $\frac{1}{en}\nabla_\parallel n T_e$ the pressure gradient, $\frac{0.71}{e}\nabla_\parallel T_e$ the temperature gradient, and $\nabla_\parallel \phi$ the electric field. The definitions of radial and perpendicular current are from the sum of (ion and electron) momentum balance equations. The total energy for ions is calculated as

$$\frac{d}{dt}\left(\frac{3}{2} n_i T_i + \frac{m_i n_i}{2} \mathbf{v}_i^2\right) + \nabla \cdot \left[\left(\frac{5}{2} n_i T_i + \frac{m_i n_i}{2} \mathbf{v}_i^2\right)\mathbf{v_i} + \Pi_i \mathbf{v}_i + \mathbf{q_i}\right] = (Z_i e n_i \mathbf{E} - \mathbf{R}_i) \cdot \mathbf{v}_i - Q_{ei} + S_{Ei}, \tag{12}$$

while the electron energy conservation is given as

$$\frac{d}{dt}\left(\frac{3}{2} n_e T_e\right) + \nabla \cdot \left(\frac{5}{2} n_e T_e \mathbf{v}_i + \mathbf{q}_e\right) = -e n_e \mathbf{E} \cdot \mathbf{v}_e + \mathbf{R}_i \cdot \mathbf{v}_i + Q_{ei} + S_{ee}. \tag{13}$$

In the equations, $\mathbf{q}_e$ and $\mathbf{q_i}$ are the electron and ion energy fluxes, Q_{ei} represents the coupling between electrons and ions, i.e., the collisional equilibration term, while the terms S_{ni}, $S_{m_i v_{i\parallel}}$ and S_{Ei} are sources for particles, momentum, and energy due to neutral and are calculated by the Monte Carlo code.

B2.5 is self-consistently coupled with Eunomia, implying that the static plasma background characterizing Eunomia standalone is now calculated and updated by B2.5 for every cycle, while Eunomia provides sources and sinks for ion and electron energy, particle density, and momentum. A graphical representation is shown in Fig. 11.

In this work, a new grid representing the upgraded linear machine Magnum-PSI has been used and can be seen in Fig. 12. All walls are reflecting walls for the test particle, and the velocity of the

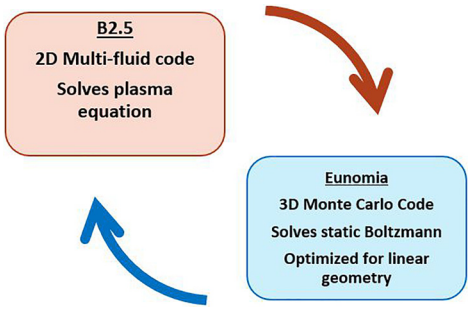

FIG. 11. Graphical representation of the iteration scheme between the two codes, reciprocally providing information on the plasma itself (B2.5 for Eunomia) and sources and sinks for particles, momentum and energy (Eunomia for B2.5).

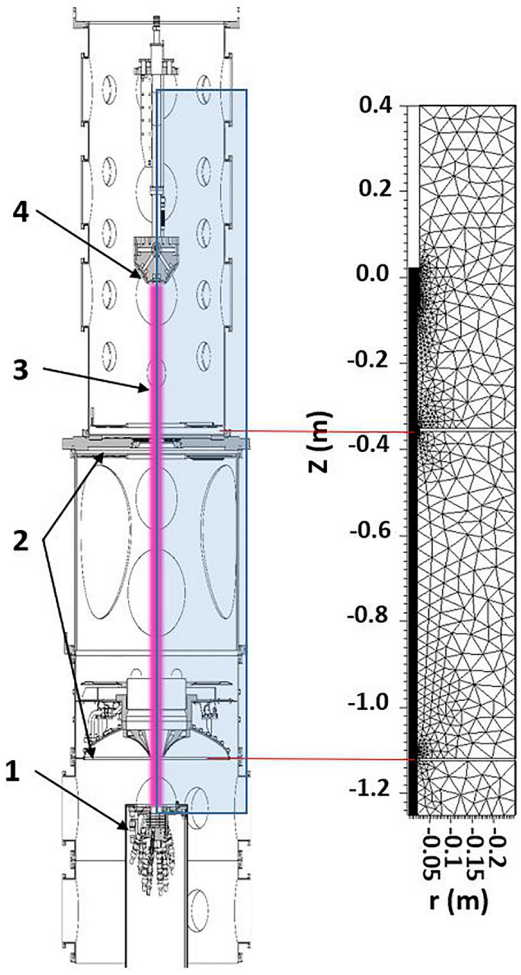

FIG. 12. (Right): Drawing of Magnum-PSI, where (1) is the plasma source, (2) the skimmers, (3) the plasma beam, and (4) the target. On the left, the geometry used in the simulations of the couple codes is shown.

reflected particle follows a cosine distribution. Moreover, the outer walls thermalize the reflected particle; therefore, the velocity is rescaled to the wall temperature. The skimmers do not thermalize the particle. Differential pumping is treated in the code as follows: a certain probability rate describes whether the test particle is terminated when crossing this boundary is specified. If that would not be the case, it gets reflected. The probability rate is updated each cycle according to the specified pressure in a specified location within the domain. To achieve the differential pumping, we have different pumps in different locations for each of the pumps.

B. Implementation of the codes

The implemented processes regarding N_2-H_2 are listed in Table IV. To get to such a reduced scheme, an extensive global plasma model has been first made. An internal validation of the code, implying a quantitative comparison of the species densities between the fully extended model with the reduced one, has been carried out for three different cases of study. Plasma scenarios were set at $T_e(1) = 0.8\,eV$ and $n_e(1) = 6 \times 10^{19}\ m^{-3}$, $T_e(2) = 1.2\,eV$ and $n_e(2) = 2.6 \times 10^{20}\ m^{-3}$, and $T_e(3) = 1.8\,eV$ and $n_e(3) = 3.5 \times 10^{20}\ m^{-3}$ respectively. Results clearly showed consistency between the two sets. More details on such a procedure can be found in Ref. 27. It is worth mentioning that the plasma chemical tables presented hereafter have been implemented keeping the ones in Table III fully activated.

TABLE IV. Processes included in B2.5-Eunomia to study nitrogen-seeding hydrogen plasma detachment scenarios.

No.	Reaction	Type	References
12	$N_2 + e^- \rightarrow N + N + e^-$	Dissociation	53
13	$H_2 + N \rightarrow NH + H$	Atomic transfer	54
14	$N_2 + H_2^+ \rightarrow N_2H^+ + N$	Proton transfer	39
15	$N_2H^+ + e^- \rightarrow N_2 + H$	Dissociative recombination	55
16	$N_2H^+ + e^- \rightarrow NH + N$	Dissociative recombination	55
17	$N + e^- \rightarrow N^+ + 2e^-$	Ionization	56
18	$NH + H^+ \rightarrow NH^+ + H$	Ion conversion	57
	$NH^+ + e^- \rightarrow N + H$	Dissociative recombination (N-MAR)	41
19	$N + e^- \rightarrow N + e^-$	Elastic collision	BGK
20	$N_2 + e^- \rightarrow N_2 + e^-$	Elastic collision	BGK
21	$NH + H_2 \rightarrow NH + H_2$	Elastic collision	BGK
22	$NH + H \rightarrow NH + H$	Elastic collision	BGK
23	$NH + N_2 \rightarrow NH + N_2$	Elastic collision	BGK
24	$NH + N \rightarrow NH + N$	Elastic collision	BGK
25	$H_2 + H_2 \rightarrow H_2 + H_2$	Elastic collision	BGK
26	$H_2 + N_2 \rightarrow H_2 + N_2$	Elastic collision	BGK
27	$N_2 + N_2 \rightarrow N_2 + N_2$	Elastic collision	BGK
28	$H + N \rightarrow H + N$	Elastic collision	BGK
29	$H + H \rightarrow H + H$	Elastic collision	BGK
30	$N + N \rightarrow N + N$	Elastic collision	BGK
31	$N + N_2 \rightarrow N + N_2$	Elastic collision	BGK
32	$H_2 + N \rightarrow H_2 + N$	Elastic collision	BGK
33	$N_2 + H \rightarrow N_2 + H$	Elastic collision	BGK

TABLE V. Processes included in B2.5-Eunomia to study helium-seeding hydrogen plasma detachment scenarios.

No.	Reaction	Type	References
34	$He + e^- \rightarrow He^*(2^3S) + e^-$	Excitation	58
35	$He^*(2^3S) \rightarrow He + h\nu$	Radiative relaxation	58
36	$He^*(2^3S) + e^- \rightarrow He^+ + 2e^-$	Ionization	58
37	$He + e^- \rightarrow He^+ + 2e^-$	Ionization	58
38	$He^+ + e^- \rightarrow He$	Recombination	56
39	$He + e^- \rightarrow He + e^-$	Elastic collision	BGK
40	$He + H_2 \rightarrow He + H_2$	Elastic collision	BGK
41	$He + H \rightarrow He + H$	Elastic collision	BGK
42	$He + H^+ \rightarrow He + H^+$	Elastic collision	BGK

For what concerns simulations regarding He/H_2 puffing in the target chamber, other processes have been added in the code. These are listed in Table V.

Finally, the reactions implemented for the H_2/Ar seeding case are reported in Table VI.

In B2.5-Eunomia, the rate for hydrogenic collisions has been taken from AMJUEL[56] and HYDEL databases, which are the ones also used by default in the Eirene code. For the newly added reactions, the reference for the rate is listed. The cross section for neutral-neutral elastic collisions is calculated by using the BGK approximation method[59] and is based on the Lennard-Jones potential. For electron-driven processes, the rate is calculated by the code as a function of the local (per-cell) electron temperature and density. Molecule-assisted-recombination mechanisms, i.e., reactions (8), (9), and (17) are treated in such a way that the rate-determining step is the ion conversion. The products of that process are assumed to instantaneously recombine with an electron.

C. Simulating plasma detachment in Magnum-PSI by means of B2.5-Eunomia codes

In this section, we present numerical simulations concerning the modeling of the full geometry of linear machine Magnum-PSI. For the first time, couple codes B2.5 and Eunomia have been used to specifically study detachedlike experimental scenarios with newly

TABLE VI. Processes included in B2.5-Eunomia to study Argon-seeding hydrogen plasma detachment scenarios.

No.	Reaction	Type	References
43	$Ar + e^- \rightarrow Ar^+ + 2e^-$	Excitation	56
44	$Ar^+ + e^- \rightarrow Ar$	Recombination	56
45	$Ar + Ar \rightarrow Ar + Ar$	Elastic collision	BGK
46	$Ar + H \rightarrow Ar + H$	Elastic collision	BGK
47	$Ar + H_2 \rightarrow Ar + H_2$	Elastic collision	BGK
48	$Ar + H^+ \rightarrow Ar + H^+$	Elastic collision	BGK

implemented plasma chemistry. The scope of this exercise is to gain more knowledge on the physics and chemistry occurring during experiments. The authors would like to underline that these simulations have to be considered as code experiments rather than predictive models to be quantitatively benchmarked with experimental data.

D. Modeling results

The baseline scenario, i.e., attached plasma conditions, have been set up without any external neutral source (gas puffing) and the achieved background neutral pressure in the target chamber corresponds to ≈0.3 Pa. As can be seen in Fig. 13(a), the plasma beam is conserved throughout its whole path in the target chamber. In particular, we can observe a peak in the electron density in the vicinity of the target. This is due to ion recycling at the wall, which leads to desorption of neutrals that are promptly ionized. In attached plasma conditions, the plasma environment near the wall is in the so-called high recycling regime. Similar findings have been described in Ref. 60, where simulations with SOLEDGE2D-EIRENE[61] suite have been carried out for linear plasma device Pilot-PSI.

In Fig. 13(b), a detached plasma scenario has been obtained by actively puffing H_2 in the target chamber. The resulting background neutral pressure is ≈2 Pa. The seeding location is depicted by the red circle in Fig. 13. The "gaseous chamber" concept, which has been experimentally studied with several linear machines, as described in Ref. 16, has been successfully replicated in this simulation. As can be observed, n_e quickly drops once the beam enters the target chamber, passing from $\approx 5 \times 10^{19}$ m^{-3} to $\approx 1 \times 10^{19}$ m^{-3}. A further

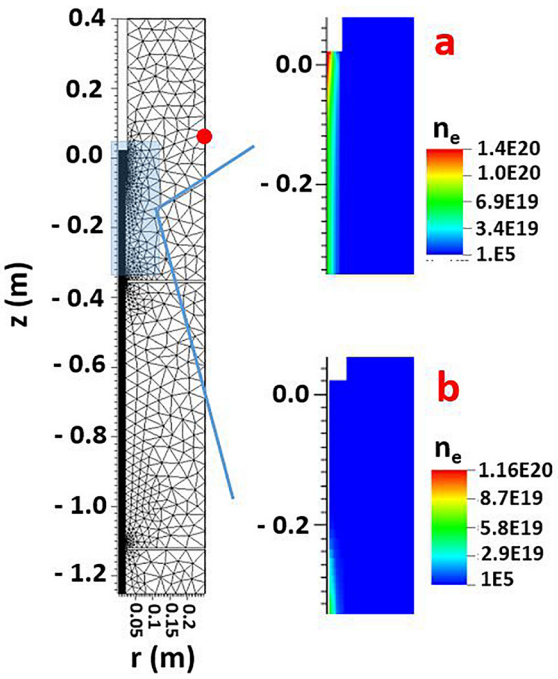

FIG. 13. Comparison between attached (a) and detached (b) plasma scenarios. On the left, the highlighted region (in blue) corresponds to the volume between the skimmer and the target. The red circle is the puffing location in the simulations.

characteristic feature of detachment, compared to the attached case, is the plasma pressure drop led by momentum loss and volume recombination processes.

Dedicated code-experiments have been carried out in order to study the difference between He, Ar, and N_2 puffing, together with H_2, at different mixing ratios. In principle, we replicated the experiments presented in Sec. IV. The novelty of this exercise lays in the fact that new plasma chemical processes have been included in a kinetic-fluid coupled code. The aim is to highlight possible different volume-driven effects on plasma detachment. In particular, the role of the reactive N_2-related NH radical and N-MARs is of great interest, given that NH_x molecules are surely produced in the divertor. The particle source for NH has been set assuming a conversion efficiency of nitrogen to ammonia (molecular precursor for the NH radical) of 7%, which is in line with previous studies.[62,63] NH_x particles are formed via the surface process; while N_2 is injected in the location depicted in Fig. 13, the source for NH has been set at the target plate.

The total plasma pressure modeled at 3 cm in front of the target, together with the heat flux (at the sheath entrance) calculated as in Eq. (1), is reported in Fig. 14.

Plasma parameters achieved with the simulations are about on the order of $n_e \approx 10^{19}$ m^{-3} with electron temperatures below 1 eV. Although a quantitative comparison between experiments and simulations is beyond the scope of this work, the same trend is obtained when comparing Magnum-PSI results with the model.

The presence of nitrogen seeding in combination with H_2 leads to a net decrease in the plasma pressure by roughly 35%. This value may be overestimated due to the fact that NH (electron donor responsible for the first step of N-MAR) is injected entirely from the surface of the target. Regarding H_2 + Ar and H_2 + He puffing scenarios, a reversed effect is achieved. In fact, plasma pressure increases by ≈20% in both cases, reducing the effectiveness of detachment. No significant differences are recorded between He and Ar scans, indicating that the absence of impurity-induced volume recombination processes might lead to a dilution effect of H_2 in the plasma parameter range characterizing these simulations. The heat flux, calculated at the sheath edge with no presheath or sheath effects taken into account, provided the same trend. It is worth underlining that a full description of the sheath physics is beyond the capabilities of B2.5. No significant plasma radial transport occurs along the different scans for He, Ar, and N_2 cases of study.

These results confirm that adding inert species into the puffed mixture does not have beneficial effects for detachment in the vicinity of the target. An increase in plasma pressure leads to an enhanced particle flux, hence to a higher heat flux to the target.

To address the contribution of N-MAR and MAR, respectively, the collision frequency of these recombination processes for a 10% N_2 seeding case has been monitored and is shown in Fig. 15.

The N-MAR process occurs extensively in the vicinity of the target (axially) and radially along the whole beam, while it becomes negligible when moving far away from the plate at about 5 cm. The spatial distribution of such process represents a clear indication of the enhanced recombination of incoming hydrogen ions before they reach the target.

Regarding the purely hydrogenic process, hardly any MAR events appear to be occurring in the simulation. The vibrational excited states of H_2, which are needed for the first ion conversion step of MAR, are

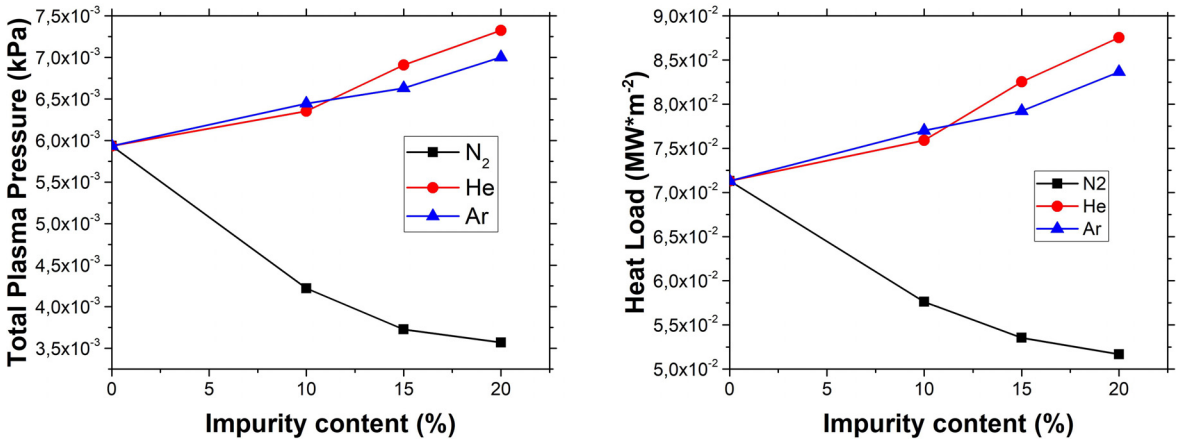

FIG. 14. Left: Modeled total plasma pressure. Right: heat load.

simulated in the code. Nevertheless, the contribution of this two-step reaction does not seem to be relevant in the conditions examined. That might be due to the low T_e (<1 eV), which is given by the code as an output.

The main lack of this model and, to the knowledge of the authors, of any other H_2-N_2 plasma code, is the absence of a scaling law for the following process: $H^+ + N_2(v) \rightarrow H + N_2^+$, which is a further recombination path for H^+. It is fair to assume that a large fraction of injected N_2 molecules undergo electron-impact vibrational excitation [threshold energy for $N_2(v=0 \rightarrow v=1)$ is 0.29 eV]. To provide a description of the entire plasma chemistry going on in a detachedlike hydrogen plasma with N_2 seeding, and therefore to make quantitative predictions, a dedicated study on the role of $N_2(v)$ would be needed.

Moreover, to carry out quantitative comparison between experiments and simulations with B2.5-Eunomia, dedicated studies on the "free parameters" currently assumed in the code, e.g., cross field transport coefficients, potential boundary, and plasma flow from the source should be carried out. Nevertheless, the newly implemented plasma chemistry is responsible for the achieved trends, indicating that the presence (or the absence) of further ion-recombination paths, that differ from the pure hydrogenic ones, may have positive influence in reducing the particle flux during detachment. Specifically, the role of N-MAR is hereby highlighted experimentally and confirmed with numerical simulations. Therefore, that process should be included in the state-of-the-art divertor-relevant plasma physics codes.

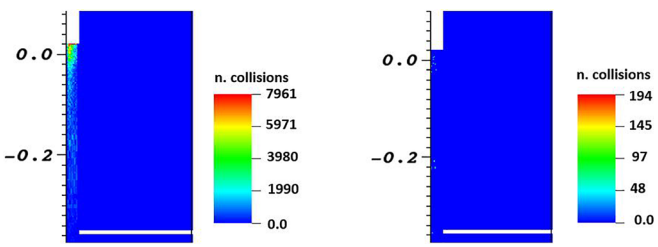

FIG. 15. N-MAR (left) and MAR (right) collision frequency.

VII. CONCLUSIONS AND OUTLOOK

The effect of different impurities on plasma detachment has been studied by means of both experiments and numerical simulations. Experiments highlighted the beneficial role of N_2, seeded together with H_2 in the target chamber, compared to He + H_2 and Ar + H_2, which showed an opposite trend. In the N_2-seeding case, a plasma pressure decrease and a reduced heat load collected at the target plate are observed, while in the remaining two cases, i.e., Ar and He, detachment performance is lowered. The plasma chemistry occurring in divertor-relevant plasma detached scenarios has been studied by means of global plasma modeling and the subsequent reduced sets of chemical equations have been implemented in the coupled code B2.5-Eunomia. Simulation results qualitatively reproduce the experimental findings, confirming the relevance of N-induced volume recombination processes (N-MAR). Moreover, a comparison between the well-known hydrogenic MAR and N-MAR has been performed, pointing out the significance of the latter in converting hydrogen ions to neutrals via molecule-assisted process. Nitrogen-related volume processes should thus be included in divertor and plasma-edge codes, N-MAR being an efficient route for the neutralization of hydrogen ions.

In the perspective of a detached plasma in a tokamak, this study focuses on the last portion of the SOL, between the ionization front and the divertor plate. A one-to-one comparison between a linear plasma device and a real divertor might be misleading. Nevertheless, results presented in this work show a heat flux reduction of about 20%, compared to pure H_2, when nitrogen (and therefore N-MAR) is introduced in the simulated environment.

Concerning these species in ITER, one of the crucial issues is the formation of tritiated ammonia, where tritium atoms bond with nitrogen and are, therefore, taken out from the system. Although no ultimate solution of such a problem has been given so far, a possibility to recover tritium might be by applying a catalytic reactor suited for isotope exchange processes at the end of the divertor pump. In this way, tritium might be recovered and could, subsequently, be re-emitted in the plasma.

ACKNOWLEDGMENTS

This work has been carried out within the framework of the EUROfusion Consortium and has received funding from the Euratom research and training program 2014–2018 and 2019–2020 under Grant Agreement No. 633053. The views and opinions expressed herein do not necessarily reflect those of the European Commission.

REFERENCES

[1]R. A. Pitts *et al.*, "Physics basis and design of the ITER plasma-facing components," J. Nucl. Mater. **415**(1 SUPPL), S957–S964 (2011).
[2]P. Stangeby, *The Plasma Boundary of Magnetic Fusion Devices* (Institute of Physics Publishing, 2000).
[3]S. I. Krasheninnikov, A. Pigarov, and T. K. Soboleva, "Plasma-neutral gas interaction in a tokamak divertor: Effects of hydrogen molecules and plasma recombination," J. Nucl. Mater. **241–243**, 283–287 (1997).
[4]G. DeTemmerman, "Plasma—surface interactions under high heat and particle fluxes," Acta Polytech. **53**(2), 142–147 (2013).
[5]S. I. Krasheninnikov, A. S. Kukushkin, and A. A. Pshenov, "Divertor plasma detachment," Phys. Plasmas **23**(5), 055602 (2016).
[6]A. Loarte *et al.*, "Chapter 4: Power and particle control," Nucl. Fusion **47**(6), S203–S263 (2007).
[7]Y. U. S. Takamura, N. Ohno, and D. Nishijima, "Generation and characteristics of detached recombining plasma and its dynamic behaviour a bridge between fusion plasmas and low-temperature ionized gases," J. Nucl. Mater. **313–316**(1), A42–A48 (2002).
[8]Y. Hayashi, "Plasma detachment study of high density helium plasmas in the Pilot-PSI device," Nucl. Fusion **56**, 126006 (2016).
[9]D. E. Post, "A review of recent developments in atomic processes for divertors and edge plasmas," J. Nucl. Mater. **220–222**, 143–157 (1995).
[10]A. A. Pshenov, A. S. Kukushkin, and S. I. Krasheninnikov, "Energy balance in plasma detachment," Nucl. Mater. Energy **12**, 948–952 (2017).
[11]A. Loarte, R. D. Monk, and J. R. Mart, "Plasma detachment in JET Mark I divertor experiments," Nucl. Fusion **38**, 331 (1998).
[12]O. Gruber *et al.*, "Observation of continuous divertor detachment in H-mode discharges in ASDEX Upgrade," Phys. Rev. Lett. **74**(21), 4217–4220 (1995).
[13]M. Oberkofler *et al.*, "First nitrogen-seeding experiments in JET with the ITER-like wall," J. Nucl. Mater. **438**(SUPPL), S258–S261 (2013).
[14]A. Kallenbach *et al.*, "Plasma surface interactions in impurity seeded plasmas," J. Nucl. Mater. **415**(1 Suppl), S19–S26 (2011).
[15]A. Kallenbach, M. Bernert, R. Dux, L. Casali, T. Eich, and L. Giannone, "Impurity seeding for tokamak power exhaust: From present devices via ITER to DEMO," Plasma Phys. Controlled Fusion **55**, 124041 (2013).
[16]N. Ohno, "Plasma detachment in linear devices," Plasma Phys. Controlled Fusion **59**(3), 034007 (2017).
[17]H. J. N. Van Eck *et al.*, "High-fluence and high flux performance characteristics of the superconducting Magnum-PSI linear plasma facility," Fusion Eng. Des. **142**, 26–32 (2019).
[18]J. Rapp *et al.*, "Construction of the plasma-wall experiment Magnum-PSI," Fusion Eng. Des.. **85**(7–9), 1455–1459 (2010).
[19]T. W. Morgan *et al.*, "A high-repetition rate edge localised mode replication system for the Magnum-PSI and Pilot-PSI linear devices," Plasma Phys. Controlled Fusion **56**, 095004 (2014).
[20]G. J. Van Rooij *et al.*, "Extreme hydrogen plasma densities achieved in a linear plasma generator," Appl. Phys. Lett. **90**(12), 121501 (2007).
[21]H. J. N. Van Eck *et al.*, "Pre-design of Magnum-PSI: A new plasma–Wall interaction experiment," Fusion Eng. Des. **82**, 1878–1883 (2007).
[22]G. J. Van Rooij, "Thomson scattering at Pilot-PSI and Magnum-PSI," Plasma Phys. Controlled Fusion **51**, 124037 (2009).
[23]G. G. Van Eden *et al.*, "Plasma radiation studies in Magnum-PSI using resistive bolometry," Nucl. Fusion **58**(10), 106006 (2018).
[24]A. Schumack, "The influence of electric fields and neutral particles on the plasma sheath at ITER divertor conditions," Ph.D. thesis (Eindhoven University of Technology, 2011).
[25]T. Body *et al.*, "A volume-averaged model of nitrogen-hydrogen plasma chemistry to investigate ammonia production in a plasma-surface-interaction device," Plasma Phys. Controlled Fusion. **60**(7), 075011 (2018).
[26]R. Perillo *et al.*, "Experimental evidence of enhanced recombination of a hydrogen plasma induced by nitrogen seeding in linear device Magnum-PSI," Nucl. Mater. Energy **19**, 87–93 (2019).
[27]R. Perillo *et al.*, "Studying the influence of nitrogen seeding in a detached-like hydrogen plasma by means of numerical simulations," Plasma Phys. Controlled Fusion **60**(10), 105004 (2018).
[28]K. Verhaegh, *Spectroscopic Investigations of Detachment on TCV* (University of York, 2018).
[29]N. Ezumi *et al.*, "Synergistic effect of nitrogen and hydrogen seeding gases on plasma detachment in the GAMMA 10/PDX tandem mirror," Nucl. Fusion **59**, 066030 (2019).
[30]S. Abe, S. C. Thakur, R. P. Doerner, and G. R. Tynan, "Hydronitrogen molecular assisted recombination (HN-MAR) process in ammonia seeded deuterium plasmas," Nucl. Mater. Energy **19**, 390–396 (2019).
[31]A. Hurlbatt *et al.*, "Concepts, capabilities, and limitations of global models: A review," Plasma Processes Polym. **14**(1), 1600138 (2017).
[32]J. Van Dijk, K. Peerenboom, M. Jimenez, D. Mihailova, and J. Van Der Mullen, "The plasma modelling toolkit Plasimo," J. Phys. D: Appl. Phys **42**(19), 194012 (2009).
[33]W. Graef, "Zero-Dimensional Models for Plasma Chemistry," Ph.D. thesis (Eindhoven University of Technology, 2012).
[34]J.-S. Yoon *et al.*, "Cross sections for electron collisions with hydrogen molecules," J. Phys. Chem. Ref. Data **37**(2), 913–931 (2008).
[35]R. K. Janev, W. D. Langer, D. E. J. Post, and K. J. Evans, Jr., *Elementary Processes in Hydrogen-Helium Plasmas: Cross Sections and Reaction Rate Coefficients* (Springer, 1987), Vol. 4, p. 4.
[36]M. D. Shah, "Pulsed crossed-beam study of the ionisation of atomic hydrogen by electron impact," J. Phys. B **20**, 3501 (1987).
[37]I. Bray and T. Stelbovicsi, "Calculation of the total ionization cross section and spin asymmetry in electron-hydrogen scattering from threshold to 500 eV," Phys. Rev. Lett. **70**, 746 (1993).
[38]S. J. Buckman, A. V. Phelps, J. Buckman, and A. V. Phelpsb, "Vibrational excitation of D2 by low energy electrons vibrational excitation of O 2 by low energy electrons," J. Chem. Phys. **82**, 4999 (1985).
[39]V. G. Anicich, "Evaluated bimolecular ion-molecule gas phase kinetics of positive ions for use in modeling planetary atmospheres, cometary comae, and interstellar clouds," J. Phys. Chem. Ref. Data **22**(6), 1469–1569 (1993).
[40]C. H. Kruger, "Nonequilibrium effects in thermal plasma chemistry," Plasma Chem. Plasma Process. **9**(4), 435–443 (1989).
[41]J. Brian, "The dissociative recombination of molecular ions," Phys. Rep. **186**(5), 215–248 (1990).
[42]B. J. McCall *et al.*, "Dissociative recombination of rotationally cold H3+," Phys. Rev. A **70**(5), 52716 (2004).
[43]S. Oh, H. Lee, C. Chung, S. Oh, H. Lee, and C. Chung, "Global model including multistep ionizations in helium plasmas," Phys. Plasmas **23**(12), 123508 (2016).
[44]W. L. Morgan, http://www.lxcat.laplace.univ-tlse.fr for Morgan database, 2012.
[45]A. T. Hjartarson, "Low pressure hydrogen discharges diluted with argon explored using a global model," Plasma Sources Sci. Technol. **19**, 65088 (2010).
[46]M. Sode, T. Schwarz-Selinger, and W. Jacob, "Ion chemistry in H2-Ar low temperature plasmas," J. Appl. Phys. **114**(6), 063302 (2013).
[47]R. C. Wieggers, P. W. C. Groen, H. J. de Blank, and W. J. Goedheer, "Simulation of the neutral inventory in the Piot-PSI beam," Contrib. Plasma Phys. **52**(5–6), 440–444 (2012).
[48]K. Jesko, Y. Marandet, H. Bufferand, J. P. Gunn, and H. J. Van Der Meiden, "Soledge2D-Eirene simulations of the Pilot-PSI linear plasma device compared to experimental data," Contrib. Plasma Phys. **58**, 6–8 (2018).
[49]B. De Groot *et al.*, "Extreme hydrogen plasma fluxes at Pilot-PSI enter the ITER divertor regime," Fusion Eng. Des. **82**, 1861–1865 (2007).
[50]R. Wiggers, "B2.5-Eunomia simulations of Pilot-PSI," Ph.D. thesis (Eindhoven University of Technology, 2012).
[51]R. Schneider, X. Bonnin, K. Borrass, D. P. Coster, H. Kastelewicz, and D. Reiter, "Plasma edge physics with B2-Eirene," Contrib. Plasma Phys. **191**(1), 3–191 (2006).

[52]S. I. Braginskii, "Transport processes in a plasma," Rev. Plasma Phys. **1**, 205–311 (1965).
[53]Y. Itikawa, "Cross sections for electron collisions with nitrogen molecules," J. Phys. Chem. Ref. Data **35**(1), 31–53 (2006).
[54]M. Koshi *et al.*, "Reactions of N(^{4}S) atoms with NO and H_2," J. Chem. Phys. **93**(12), 8703 (1990).
[55]T. Amano, "The dissociative recombination rate coefficients of H_3^+, HN_2^+, and HCO^+," J. Chem. Phys. **92**(11), 6492–6501 (1990).
[56]D. Reiter, The data file AMJUEL: Additional atomic and molecular data for EIRENE FZ, Forschungszentrum Julich GmbH FRG, Version: April 26, 2011 Available via E-mail from d.reiter@fz-juelich.de (2011), pp. 1–393.
[57]S. S. Prasad and W. T. Huntress, "A model for gas phase chemistry in interstellar clouds. I—The basic model, library of chemical reactions, and chemistry among C, N, and O compounds," Astrophys. J. Suppl. Ser. **43**, 1 (1980).
[58]G. Park, H. Lee, G. Kim, and J. K. Lee, "Global Model of He/O_2 and Ar/O_2 atmospheric pressure glow discharges," Plasma Processes Polym. **5**, 569–576 (2008).
[59]P. L. Bhatnagar, E. P. Gross, and M. Krook, "A model for collision processes in gases. I. Small amplitude processes in charged and neutral one-component systems," Phys. Rev. **94**(3), 511–525 (1954).
[60]K. Jesko, Y. Marandet, H. Bufferand, and J. P. Gunn, "Studying divertor relevant plasmas in the Pilot-PSI linear plasma device: Experiments versus modelling," Plasma Phys. Controlled Fusion **60**, 125009 (2018).
[61]H. Bufferand *et al.*, "Implementation of drift velocities and currents in SOLEDGE2D—EIRENE," Nucl. Mater. Energy **12**, 852–857 (2017).
[62]V. Rohde, D. Neuwirth, M. Oberkofler, and U. Team, "Nitrogen balance and ammonia formation during nitrogen seeded discharges at ASDEX Upgrade," in 40th EPS Conference on Plasma Physics, EPS 2013 (2012), pp. 2–5.
[63]J. H. Van Helden *et al.*, "Detailed study of the plasma-activated catalytic generation of ammonia in N2-H2 plasmas," J. Appl. Phys. **101**(4), 043305 (2007).